A comprehensive analysis of the Illapel 2015 Mw8.3 earthquake from GPS and InSAR data

E. Klein [a,b,*], C. Vigny [a], L. Fleitout [a], R. Grandin [c], R. Jolivet [a], E. Rivera [d], M. Métois [e]

[a] Laboratoire de Géologie, Département de Géosciences, ENS, CNRS, UMR8538, PSL Research University, Paris, France
[b] Institut de Physique du Globe de Strasbourg, UMR7516, Université de Strasbourg, EOST, CNRS, Strasbourg, France [1]
[c] Institut de Physique du Globe de Paris, UMR 7154, Sorbonne Paris Cité, Université Paris Diderot, Paris, France
[d] Departamento de Geología, Universidad de Chile, Plaza Ercilla 803, Santiago, Chile
[e] Univ Lyon, Université Lyon 1, ENS de Lyon, CNRS, UMR 5276 LGL-TPE, Villeurbanne, France

A B S T R A C T

The September 16, 2015 Mw8.3 Illapel Earthquake occurred on a locked segment of the South American subduction in Chile. This segment ruptured during comparable size earthquakes in the past, in 1880 and 1943, suggesting a somehow regular pattern of characteristic Mw8+ earthquakes occurring every 60 to 80 yr. This recurrence is in agreement with the accumulation of elastic deformation in the upper plate due to the Nazca–South America subduction at a constant rate of 6.5 cm/yr, leading to a deficit of ∼4.5 m of slip to be released every 70 yr. Previous studies consistently imaged the distribution of co-seismic slip along the fault based on geodetic, seismological and far field tsunami data and all described a significant amount of shallow slip resulting in a large tsunami. In addition, some models highlighted an apparent mismatch between the modeled rake of slip and the direction of plate convergence, suggesting the buildup of large strike-slip deficit. Some of these important questions remain open. Is shallow slip really well resolved and substantiated? Is the apparent principal direction of slip during the earthquake really required by the geodetic data?

Here, using a comprehensive analysis of continuous GPS sites (including high rate and static displacements) and new survey data from acquired over more than 50 pre-existing sites, complemented with InSAR data, we show that the 2015 rupture overlaps very well the 1943 rupture, with the absence of significant slip south of 32°S and north of 30.2°S (peninsula Lingua de Vaca). Despite the wealth of geodetic data, the shallowest part of the subduction interface remains poorly resolved. We also show that the rake of the earthquake is fully compatible with the oblique plate convergence direction (rather than perpendicular to the trench), meaning that no subsequent trench-parallel motion is required by the data. We propose that the large Low Coupling Zone (LCZ) at the latitude of La Serena revealed by present day coupling distribution is stable over at least two seismic cycles. Inside the coupled area, peak coseismic slip is located precisely offshore the highest coastal topography and elevated terraces, adding weight to a potential correlation between the seismic cycle and long term permanent deformation. Finally, we show that early post-seismic after-slip occurs mostly down-dip of co-seismic asperity(ies), extending north and south of the 2015 rupture area.

© 2017 Elsevier B.V. All rights reserved.

1. Introduction

The September 16, Mw8.3 Illapel earthquake, occurred at 22:54:31 (UTC), on an active segment of the central Chilean subduction zone. Uncertainties and errors in magnitude estimates of past large earthquakes in the literature might conceal a sequence of Mw8+ earthquake. Although different magnitudes have been proposed for the 1943 earthquake (Mw7.9, Beck et al., 1998; 8.2, Engdahl and Villaseñor, 2002 and 8.3, Lomnitz, 2004), we consider the magnitude estimates in the most homogeneous catalog (Engdahl and Villaseñor, 2002) (Fig. 1). Therefore, using coherent re-estimations of past earthquake magnitudes, a cycle of Mw8+ earthquake every 60 to 70 yr seems to emerge with the last 3 occurring in 1880, 1943 and 2015. Superimposed on this cycle, a giant earthquake of magnitude 9 ruptured in 1730 a longer section of the subduction, including the Illapel segment (e.g. Udias et al., 2012), raising questions about a "super cycle", with larger (and

Fig. 1. Seismotectonic context of the Central Chile subduction interface. The Nazca/South-America convergence rate is represented by the red arrow. Green stars, which depict the large intraplate earthquake epicenters, and estimated historical rupture extents are based on Engdahl and Villaseñor (2002); Lomnitz (2004). Slip contour of the Maule earthquake from Klein et al. (2016); Slip contour of the Illapel earthquake is the preferred model presented in this study. Coupling model (red color scale) from Métois et al. (2016). The area of very low sensitivity is depicted by the grey area at the trench (based on sensitivity studies both for the interseismic model (Métois et al., 2016) and the coseismic model). Depth contours of the slab are extracted from the Slab1.0 model (Hayes et al., 2012). The topography and bathymetry are extracted from ETOPO5. *Inset:* localization of the study area. (For interpretation of the references to color in this figure legend, the reader is referred to the web version of this article.)

unknown) recurrence time, similar to Sumatra (Sieh et al., 2008) and Ecuador (Nocquet et al., 2016). Although the 2015 event may have closed the Illapel gap (Tilmann et al., 2016), the status of a potential larger supercycle remains unknown. Slip during the 2015 Illapel event might have delayed the occurrence of an earthquake similar to that of 1730, by releasing some of the accumulated strain. However, it might just as well have promoted it by redistributing stresses along the megathrust.

In addition to the historical seismicity, the region of Illapel is also known for its strong seismic activity over the last 20 yr. Starting in 1997, the seismic activity shows a peculiar increase, with the occurrence of six shallow thrust events, located between 30.5°S and 31.5°S during the month of July 1997 (Gardi et al., 2006; Vigny et al., 2009), until the occurrence of the Punitaqui intraplate

earthquake at 56 km depth, two months later (Lemoine et al., 2002). This Mw7.1 slab-push event has been related to a tear in the slab due to the strong accumulation of stress in the transition zone at the interface (Gardi et al., 2006). Since the Punitaqui earthquake, seventeen Mw > 6 events occurred on adjacent segments of the subduction together with regular seismic swarms. 18 yr later, the Illapel earthquake broke about 200 km of the subduction interface offshore Punitaqui.

Starting in 2004, a small scale GPS network of about 50 benchmarks has been deployed. Ten years of annual measurements revealed a highly coupled segment overlapping with the estimated rupture area of the 1943 earthquake and bordered to the north by the Low Coupled Zone (LCZ) of La Serena (Métois et al., 2012, 2014). This LCZ coincides with the northern limit of several large subduction earthquakes (i.e. 1880 and 1943). The southern boundary of this segment is unclear. Past Mw∼8 ruptures seem to have stopped near 32°S, where the Juan Fernandez ridge enters into the subduction (Yáñez et al., 2001), but no significant decrease of present day coupling can be identified there (although this was established before the 2010 Maule Earthquake) (Métois et al., 2016).

Most studies of the 2015 Illapel earthquake agree on two main characteristics. First, it appears as a characteristic earthquake, repeating those of 1880 and 1943 (e.g. Tilmann et al., 2016; Shrivastava et al., 2016; Feng et al., 2017). Second, the rupture nucleated deep on the interface, propagated updip and reached the shallow part of the interface, generating a significant tsunami (e.g. Ruiz et al., 2016; Melgar et al., 2016). Nevertheless, several issues remain.

First, daily GPS and InSAR data include coseismic displacements caused by the largest aftershock (which occurred only 25 min after the main shock) and aseismic slip that occurred during the first day. Therefore, deriving a purely coseismic deformation field for the main shock requires high rate cGPS data.

Second, the exact amount and location of shallow slip remains unclear. Geodetic data provide poor resolution over the shallowest part of the interface (the first 3 to 5 km from the trench), hence poorly constrain potential shallow slip. Therefore, if the seismic moment independently determined from seismology or tsunami records is larger than the moment inferred from geodesy alone, then slip must have occurred on the shallowest part of the interface (e.g. Hill et al., 2012). But one can also wonder whether the approximations used in the elastic properties of the various models could not be as well responsible for the difference in the moments. We will compare potencies of different models, independent from elastic shear moduli to investigate the need for significant shallow slip.

Third, previous studies in agreement with the USGS focal mechanism (http://earthquake.usgs.gov/earthquakes/eventpage/us20003k7a#moment-tensor; Duputel et al., 2012) assume a slip vector perpendicular to the trench. This led to an apparent strike slip deficit (e.g. Tilmann et al., 2016) due to the obliquity of the convergence between the Nazca and South America plates (e.g. Angermann et al., 1999; Vigny et al., 2009). In such case, the resulting strike-slip deficit should be balanced by trench parallel motion, either seismically (a strike-slip earthquake) or a-seismically (a trench parallel silent slip). However, no significant partitioning of the deformation has been documented along the Illapel segment.

We carefully investigate these points using GPS data, including continuous data acquired by a dozen of cGPS stations operated over more than 10 yr in near field and newly acquired survey data over 50 benchmarks in the Illapel area. We also use SAR data acquired by the Sentinel-1A satellite. Our dataset provides snapshots of the deformation over different timescales, from seconds (HR cGPS) to days (static cGPS, InSAR) and weeks (sGPS).

2. Data

2.1. GPS data

2.1.1. High rate cGPS data processing

Among the dozen of continuous GPS stations operating in the rupture zone of the earthquake, 10 provided high rate (1 Hz) observations during the earthquake. The data are processed using the TRACK software (MIT). The station PCLM (Pichilemu), located more than 400 km away from the rupture zone is set as reference, far enough from the rupture zone not to be affected by coseismic motion during the first 500 s following the rupture initiation. We use LC combination and IGS precise orbits. We re-estimate tropospheric delays starting from hourly estimates given by static daily solutions obtained with the GAMIT software (Herring et al., 2010a). Station motions (motograms) are then filtered. We apply a sideral filter to clean the motograms from systematic errors such as orbital errors or multipath delays and high frequency random noise. The coseismic offset is estimated on the filtered motograms using a time window of 5 min before and after the main shock (Fig. S1). This way, we isolate the contribution of the main shock from that of the large aftershock that occurred 25 min later.

2.1.2. Static GPS processing

Both continuous and survey data are processed using the GAMIT/GLOBK softwares (Herring et al., 2010a, 2010b) following the classical MIT methodology (details in Supplementary material). Two different approaches are adopted to estimate the coseismic static displacement field.

For continuous data, daily position time series are computed and the coseismic offset is simply the difference between the position of the day before and the day after the earthquake (Fig. 2A–B).

For survey data, we extrapolate the position of the benchmarks at the date of the re-survey (15 to 30 days after the earthquake, depending on the markers) using the interseismic rate estimated over the last 5 yr. We do not use interseismic rates estimated over the whole pre-seismic period of measurement (2004–2014, Vigny et al., 2009), as postseismic deformation following the 2010 Maule earthquake induces an increase of up to 10% of horizontal velocity (Klein et al., 2016; Ruiz et al., 2016). The coseismic offset is then estimated by comparing the extrapolated position with the measured one (Fig. S2). We account for postseismic deformation of the Maule earthquake, non-linear in the case of the southernmost sites, in our estimates of uncertainties on preseismic velocities (more details in the Supplementary materials).

Since campaign sites were re-surveyed between two weeks and one month after the earthquake, estimated offsets are strongly affected by early afterslip (Fig. S3). In order to extract pure coseismic deformation, we quantify and remove this early postseismic signal (Fig. S4). We derive early postseismic displacements at the location of survey sites using the cubic-spline interpolation of post-seismic displacements estimated at the cGPS sites, at the time of re-survey.

Such combination of continuous and campaign GPS-derived displacements results in a uniquely dense displacement field at +1 day covering the whole rupture area (Fig. 2C–D).

2.2. InSAR data

Processed interferograms are from Grandin et al. (2016) (Fig. 3). Before the earthquake, images were acquired on August 24, 2016 for the descending track, and August 26, 2015 for the ascending track. After the earthquake, images were acquired on the September 17, 2015 for the descending track (11h after the main shock) and on the September 19, 2015 for the ascending track (3 days after).

In order to include these data in the slip inversion procedure, interferograms are downsampled using a quadtree scheme based on the optimization of the resolution along the megathrust (Fig. S5, Lohman and Simons, 2005). To account for atmospheric noise, we compute the empirical covariance of both interferograms on a restricted zone far from the epicentral area. We model this covariance with a distance dependent exponential function to build the corresponding covariance matrix (Jolivet et al., 2015).

2.3. Description of the observed deformation field

Daily static cGPS solutions show horizontal coseismic displacements converging toward the centroid of the earthquake, with a maximum of 1.5 m recorded at the coastal station of Parque Frey Jorge (71.635°W, 30.675°S). Strong horizontal deformation is visible at relatively large distances with centimetric coseismic offsets measured up to 700 km inland in Argentina (Fig. 2A). A difference of about 10% is measured between the static solution estimated on motograms and the one estimated with daily solutions, increasing to slightly less than 20% in the south of the area, close to Los Vilos (32°S), where the main aftershock occurred. The vertical displacement field exhibits a general subsidence pattern, suggesting a rather shallow source. One uplifted zone in the epicentral area (Fig. 2B) suggests localized deeper slip. In agreement with cGPS, survey coseismic displacements highlight up to 2 m of horizontal displacements at coastal sites that are perfectly parallel, albeit distant by slightly less than 50 km, constraining the along-strike extension of the rupture. While vectors estimated north of the rupture zone are clearly converging toward the source, southern sites motion deviates (almost fully westward, cf. Fig. 2C, Fig. S3). Vertical displacements estimated at survey sites confirm the cGPS pattern of general subsidence and allow to refine the extent of the localized uplifted area, from El Maiten (31.1°S) to Canela Baja (31.5°S) (Fig. 2D, Fig. S3).

Less than 25 min after the main shock, an aftershock of magnitude Mw 7 (CSN, USGS) occurred. We estimate the corresponding static displacements on the east component of the motograms of 5 stations (Fig. S6a–b). The north component could not reliably be extracted from motograms because too small compared to the noise. Nevertheless, it is a real achievement to detect and quantify the coseismic displacements of a megathrust earthquake of Mw smaller than 7.5, thanks to the thorough processing described in section 2.1.1 (Rivera, 2015). The amplitude of coseismic displacements (2–3 cm at all 5 stations, including those further inland) is compatible with the estimated seismic moment of 3.459×10^{19} N m (equivalent to Mw7). In any case, only the high rate static coseismic solution contains the pure coseismic displacement field due to the mainshock. All others solutions are affected by this aftershock, by other earthquakes and potential aseismic slip occurring during the first day.

3. Inversion methodology

We use these geodetic data to derive a model of coseismic slip. Surface displacements resulting from slip on the megathrust are computed on a Finite Element Mesh that features an overriding plate and a subducting plate. We base our set-up on the model developed by Klein et al. (2016) to study post-seismic deformation following the Maule earthquake. Both plates are 70 km thick (typical lithospheric thermal thickness) with a refined mesh. Bathymetry and slab dip-angle variations are taken into account, using the SRTM and the USGS Slab 1.0 database (Hayes et al., 2012). We define a 30 km thick continental crust and no oceanic crust. The effect of the presence of a 30 km thick crust on both sides of the fault plane is tested and presented in the Supplementary materials. Additional details about the FEM methodology can
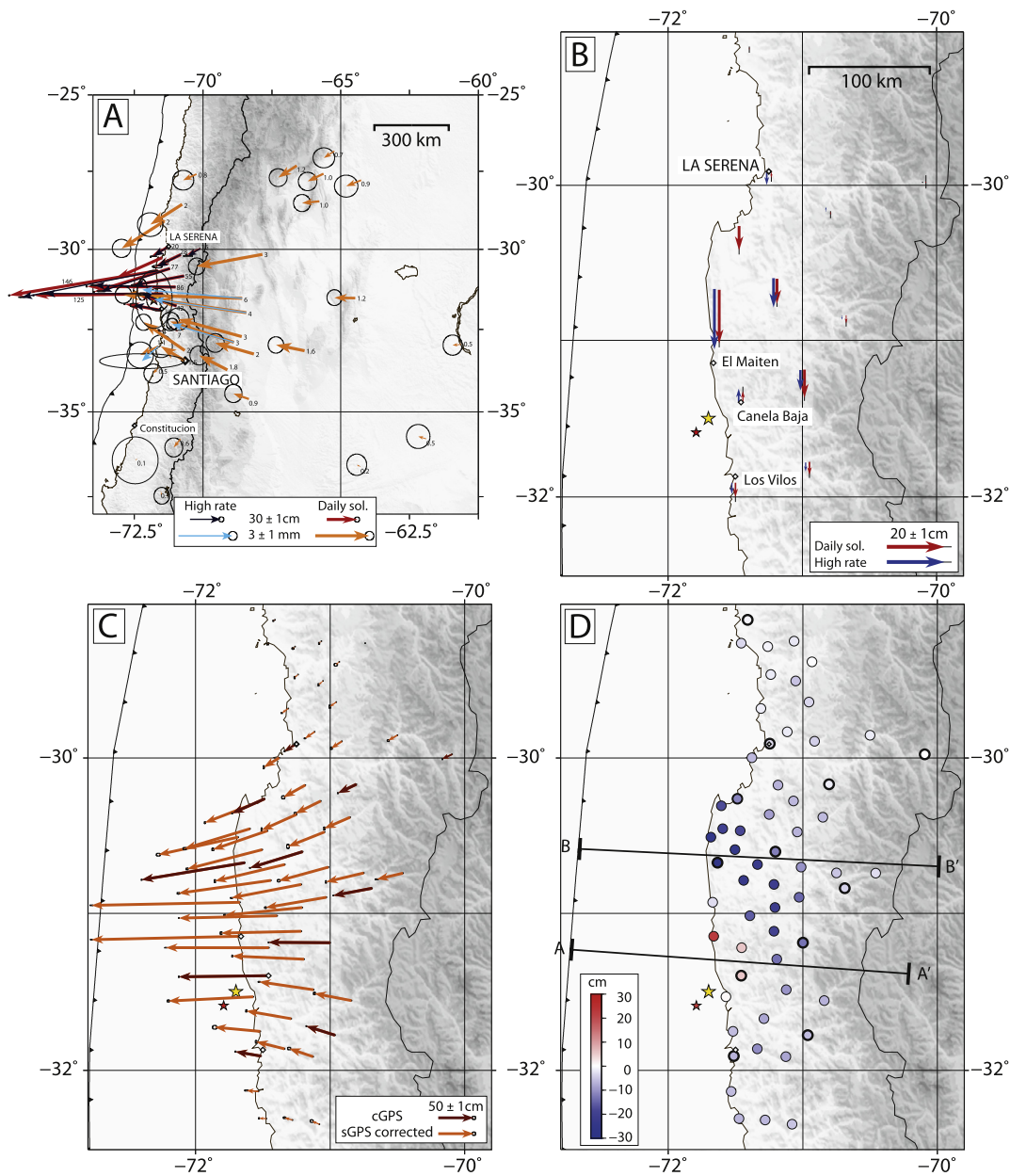
Fig. 2. Co-seismic static displacement field. For permanent sites, estimated on high rate GPS data (dark and light blue arrows) vs daily GPS data (red and orange arrows), A) on the horizontal and B) on the vertical components. Ellipses on the horizontal component depict the 95% confidence level of formal uncertainties. On the horizontal component, values reported correspond to the static daily solution. For survey sites corrected from displacements postseismic (between +1 day and the days of measurements) C) on the horizontal and D) on the vertical components. cGPS stations on the vertical map are highlighted by darker contours. Ellipses depict the 95% confidence level of formal uncertainties. The yellow star highlights the main shock epicenter, the red one, the strongest aftershock (CSN). (For interpretation of the references to color in this figure legend, the reader is referred to the web version of this article.)

be found in Klein et al. (2016). Below, the shear and bulk moduli are increasing with depth according to the Preliminary Reference Earth Model (PREM) (Dziewonski and Anderson, 1981). Along-dip and along-strike Green functions are calculated at each node of the subduction megathrust mesh. Our preferred coseismic slip distribution is determined by minimizing the L2-norm of the residuals (i.e. weighted data minus predictions). We regularize our solution by adding in the penalty function a term proportional to the square of slip on the interface scaled by a chosen damping parameter D_a. Finally the minimized function is defined as

$$(d - G \cdot m)^t \cdot C_d^{-1} \cdot (d - G \cdot m) + D_a \cdot m^t \cdot m. \qquad (1)$$

A linear trend in the E–W and N–S directions correcting the ascending and descending InSAR datasets is also inverted for. Several relative weights of cGPS, survey data and InSAR (related to the estimated variance on each of these data) have been tested.

We investigate the possible directions of earthquake slip vector (aligned or not-aligned with plate convergence) using 2 different approaches: i) As done in many previous studies, we first imposed the rake to be within 20° from the direction of steepest slope of the subduction interface (named after 'rake free'); ii) alternatively, we impose a strong penalty on the component of slip perpendicular to the convergence direction between the Nazca and South-America plates (named after 'fixed rake').

Our preferred best fit model is determined with the second method to constrain the rake and with a damping factor of 30 (Fig. 4). Survey data are downweighted by a factor of 2 with respect to cGPS data (+1 day). InSAR data (once downsampled) are downweighted by a factor of 6. For the optimal model parameter,
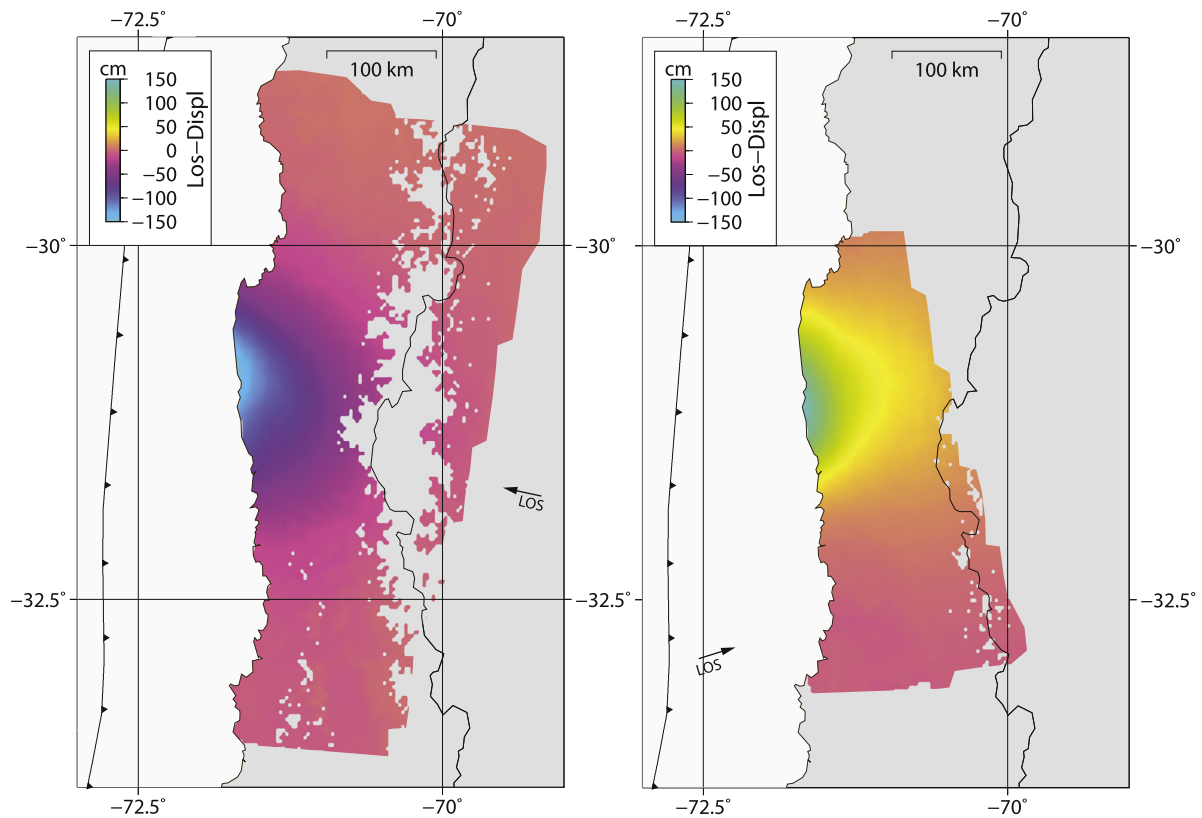
Fig. 3. Unwrapped InSAR data. Descending (left) and ascending (right) reconstructed unwrapped InSAR Sentinel-1 tracks. The LOS vector is indicated by the black arrow. Incidence angle increases from 30° in near range to 46° in far range. (For interpretation of the colors in this figure, the reader is referred to the web version of this article.)

this leads to a relative contribution to the penalty function of GPS, InSAR, slip parallel to convergence direction (damping term) and slip perpendicular to convergence direction respectively of 44%, 34%, 9% and 13%.

4. Results

4.1. Main shock co-seismic slip model

First, the main shock slip (+1 day) distribution extends over about 100 km, between 30.2°S and 31.2°S facing the Talinay Peninsula (∼30.8°S). The rupture is bounded to the north and to the south by two main structures entering the subduction: The Challenger Fracture Zone (CFZ) in the north and the Juan Fernandez Ridge (JFR) in the south. In general, the rupture correlates well with the pattern of preseismic locking (Fig. S7, Métois et al., 2016). Its northern limit coincides with the Low Coupling Zone (LCZ) of La Serena. The amount of coseismic slip is higher where coupling values are the highest (Fig. S8). Moreover, the north–south extension of the shallow area of maximum slip (30.2°–31.5°S) faces the region of elevated terraces of the Talinay peninsula (Saillard et al., 2009). The largest slip patch stretches from the hypocenter to the shallow part of the interface, following the main branch of back-projection estimated from teleseismic P-waves, which starts at the epicenter and propagates updip (Ruiz et al., 2016). The deepest part of the slip patch, responsible for the coseismic coastal uplift around 31.5°S, is aligned with a second branch of the back projection energy propagation. This second branch joins the main propagation path around 31°S, at 20 km depth, where slip increases drastically propagating updip. Our modeled peak slip is 10 m at 10 km depth with a significant decrease toward the trench (3–5 m around 8 km depth). This is consistent with the reasonable inundations reported: 4.4 m at Coquimbo tide gauge, somewhat similar to 1943 (Beck et al., 1998; Heidarzadeh et al., 2016; International
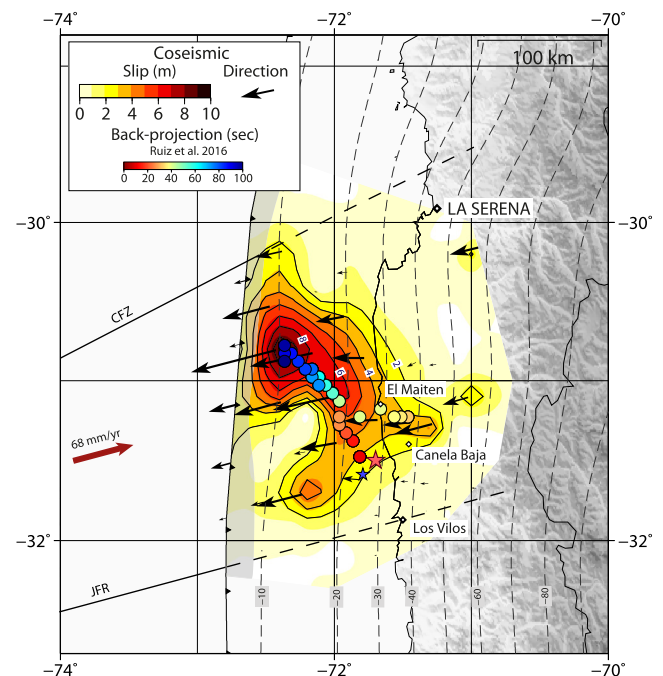
Fig. 4. Slip distribution of the preferred model of this study (red color scale), black arrows show direction of slip. Black lines represent the Challenger Fracture Zone (Contreras-Reyes and Carrizo, 2011) and the Juan Fernandez Ridge (Yáñez et al., 2001), extrapolated along the subduction interface, slab isodepths from Slab1.0 (Hayes et al., 2012). The Nazca/South-America convergence rate and direction are represented by the red arrow. The colored dots represent the locations of the sources determined from back-projection of teleseismic P-waves (Ruiz et al., 2016). The red star highlights the epicenter of the main shock. The blue star represents the epicenter's location of the largest aftershock from the CSN. The area of very low sensitivity is depicted by the grey area at the trench. (For interpretation of the references to color in this figure legend, the reader is referred to the web version of this article.)
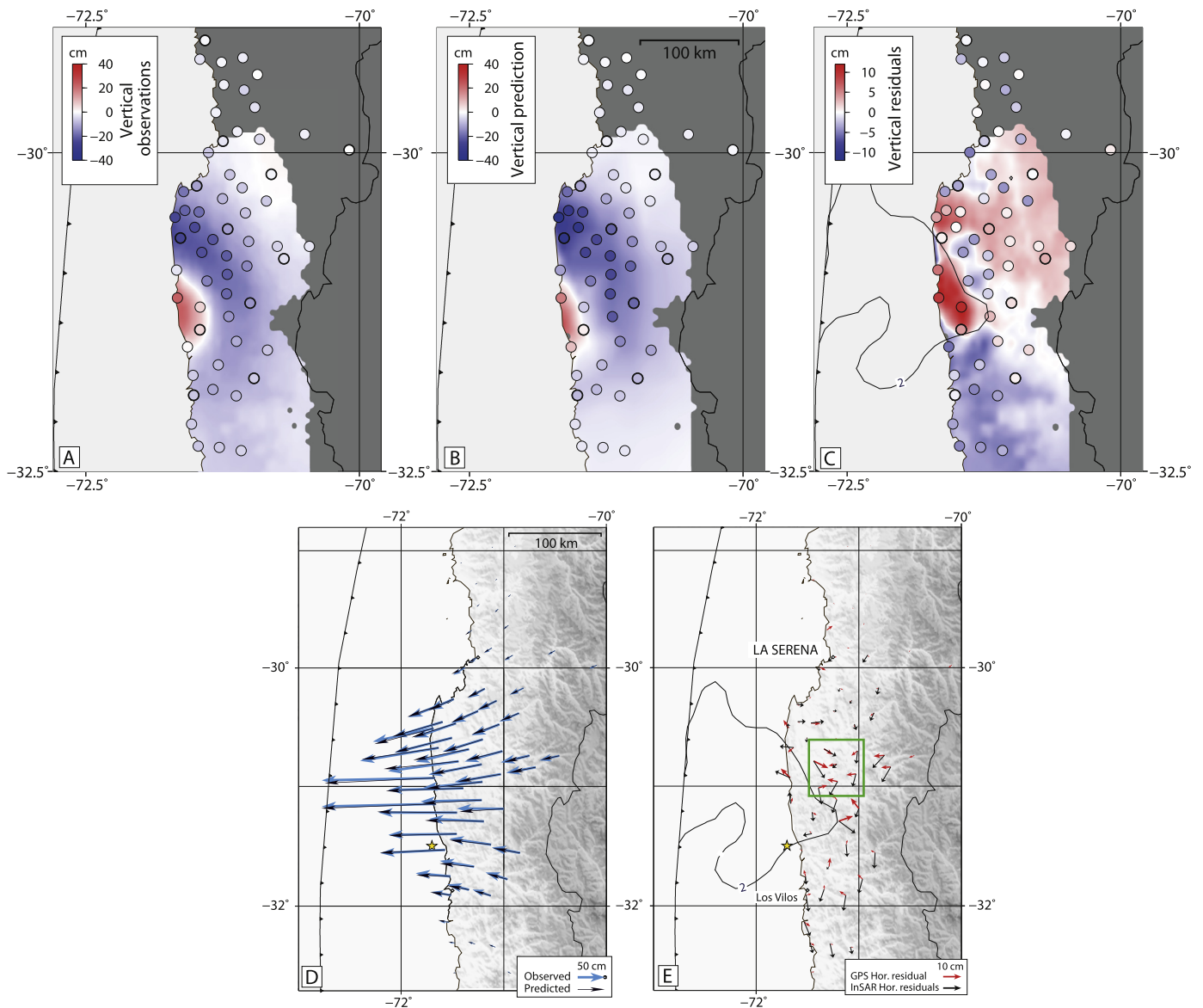
Fig. 5. Fit to data of the preferred model. A) Observed vertical coseismic displacement reconstructed from Sentinel-1 InSAR compared to observed GPS vertical displacements, B) Prediction of the preferred best fit model (from GPS and InSAR LOS components) and C) Residuals (observations – model, both GPS and InSAR). cGPS are depicted by darker contours. D) Horizontal Observed (light blue arrows) GPS static coseismic displacements (daily solution) compared to displacements predicted by the preferred model (dark blue arrows). E) Horizontal residuals (obs – mod) for GPS data (red) and for the reconstructed InSAR interpolated at the GPS stations coordinates (black). The green square highlights the area of strongest horizontal residuals. (For interpretation of the references to color in this figure legend, the reader is referred to the web version of this article.)

Tsunami Information Center (ITIC)). Our model geodetic moment is 3.42×10^{21} N m, i.e. Mw 8.29, consistent with the seismic moment of the USGS W-phase model of 3.19×10^{21} N m, i.e. Mw8.27. We show later (section 4.2) that 'true' coseismic and +1 day coseismic moments may differ by some 2×10^{20} N m.

Second, slip direction in our preferred model is aligned with the oblique plate convergence direction. Although our penalty function on the component of slip perpendicular to the convergence constrains the inversion, our model fits the data with residuals as low as those obtained with a rake free within 20° from the steepest slope direction. In contrast with previous studies using a trench perpendicular slip vector, we therefore argue that no subsequent trench-parallel motion have accumulated. Our model hence does not require slip partitioning in the Illapel segment.

Third, the slip distribution reveals a localized patch of moderate slip (∼4 m) in the region of the Mw7 aftershock slightly updip of the CSN location. We interpret the detection of slip associated with the aftershock by our inversion as an a-posteriori validation

of the chosen damping parameter: lower damping generates an artificially, unrealistic and under-constrained rough slip model while higher damping smoothes out this patch (cf. section 5.1).

Although the two LOS components of InSAR (ascending and descending tracks) have been injected in the inversion procedure, we compare the model prediction with the 3D displacement field reconstructed from the combination of across-track (LOS) and along-track (azimuth) Sentinel-1 InSAR (Grandin et al., 2016). Fits for the two LOS components are presented in Fig. S9. Our slip model reproduces well the coseismic deformation observed by GPS and InSAR (Fig. 5), with the exception of an area close to Punitaqui (highlighted by a green rectangle on Fig. 5E). There, sGPS horizontal residuals of the order of 10 cm converge toward the center of the area. Both data sets also show similar residuals on the vertical component (Fig. 5C), above the area of deep coseismic slip. Further away, vertical residuals show opposite sign between GPS and InSAR, which is due to inconsistencies between the data (Fig. 5A). InSAR also shows larger horizontal residuals south of the area
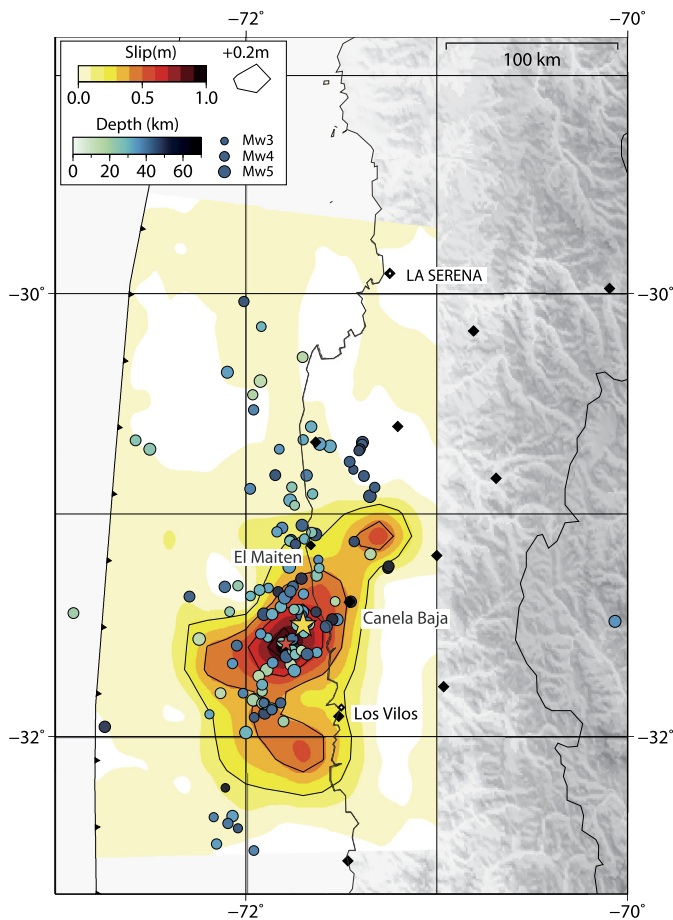
Fig. 6. Slip distribution of HF solution—daily solution. Slip distribution of the best fit model of the difference between the high rate and the daily coseismic static solutions corresponding to the main aftershock plus postseismic deformation on the first hours after the main shock (epicenter depicted by the yellow star) and the aftershock (epicenter depicted by the red star Ruiz et al., 2016). Dots represent aftershocks of Mw < 5 (CSN catalog), that occurred during the same period. Black diamonds depict the location of HR stations used. Estimated $M_0 = 2.14 \times 10^{20}$ N m (Mw = 7.5). (For interpretation of the references to color in this figure legend, the reader is referred to the web version of this article.)

(Fig. 5E and Fig. S10). Differences on the N–S component likely stem from residual noise, with amplitude of ∼10 cm, affecting the N–S component of 3-D InSAR (Grandin et al., 2016). On the other hand, differences on the U–D component, which is the best resolved by InSAR, are consistent with the fact that the InSAR ascending track was acquired 3 days after the earthquake and thus contains a non-negligible component of postseismic deformation (Fig. S11).

4.2. Early postseismic slip-model

We analyze here both the difference between the static daily and the 'high rate' displacements (Fig. 2A) and the displacement

during the first eleven days of postseismic displacements revealed by the daily solutions of the cGPS network.

Only the 'high rate' GPS data provide a true coseismic displacement. In many studies, it is the daily GPS geodetic displacements which are inverted together with seismic and tsunami data to yield the coseismic slip on the subduction interface. It is thus important to have an idea of how well these daily GPS displacements are a good approximation to the true coseismic displacement. On Fig. 6, we have inverted this difference between the daily 'coseismic' and the 'high rate' data assuming that this observed early postseismic signal is related to rapid after-slip on the subduction interface.

We quantified the early after-slip using the same inversion scheme as for co-seismic slip, described in section 3. A strong patch of after-slip is located south of the co-seismic area, consistent with the location of the main aftershock. This area coincides with the larger difference between the static offsets inferred from the high rate solution and the daily solution (Fig. 2A). The equivalent moment associated with postseismic slip during the first day is of 2.1×10^{20} N m i.e. some 7% of the true coseismic moment. The main aftershock located close to the patch of maximum after-slip has a magnitude Mw 7 and thus can account for some 15% of this first day slip.

Similarly, we have inverted the displacements observed during the first eleven days after the earthquake deduced from the daily cGPS data. We find the main postseismic slip patch downdip of the main rupture zone and slightly overlapping with the deepest zone of the larger co-seismic slip patch (Fig. 7). A second strong patch of after-slip is located south of the co-seismic area. Over the same period, the seismic activity, mainly downdip of the coseismic rupture, coincides with the slip distribution (Ruiz et al., 2016) (Fig. 7b).

5. Discussion

5.1. Influence of inversion parameters

5.1.1. Damping effect

We test here the impact of the damping parameter on the slip distribution. The damping hampers in the inverted model the contributions coming from the eigenvectors associated with the smallest eigenvalues of $G^t \cdot C_d^{-1} \cdot G$. Four slip distributions inverted with different damping coefficients (10–20–30–300) are shown on Fig. S12 and the corresponding contributions of each term in this penalty function are given in Table 1. The main difference between these four models is the amount of shallow slip. As expected given the low resolution at shallow depth, increasing damping penalizes slip on the shallowest part of the fault. Therefore, the slip distribution inverted with the lower damping coefficient has the largest amount of shallow slip (almost 8 m reaching the surface), while there is almost no shallow slip when the damping coefficient reaches 30. On the other hand, the higher the damping coefficient, the less visible the localized patch of slip attributed to the Mw7 aftershock. With the highest damping coefficient (300), the main shock and the aftershock slip distributions are merged into a single slip pattern. Regardless of the damping parameter, all

Table 1
In the 4 tested cases: contribution of each term (GPS, InSAR and damping) in the penalty function, estimation of Potency, Seismic moment and Magnitude.

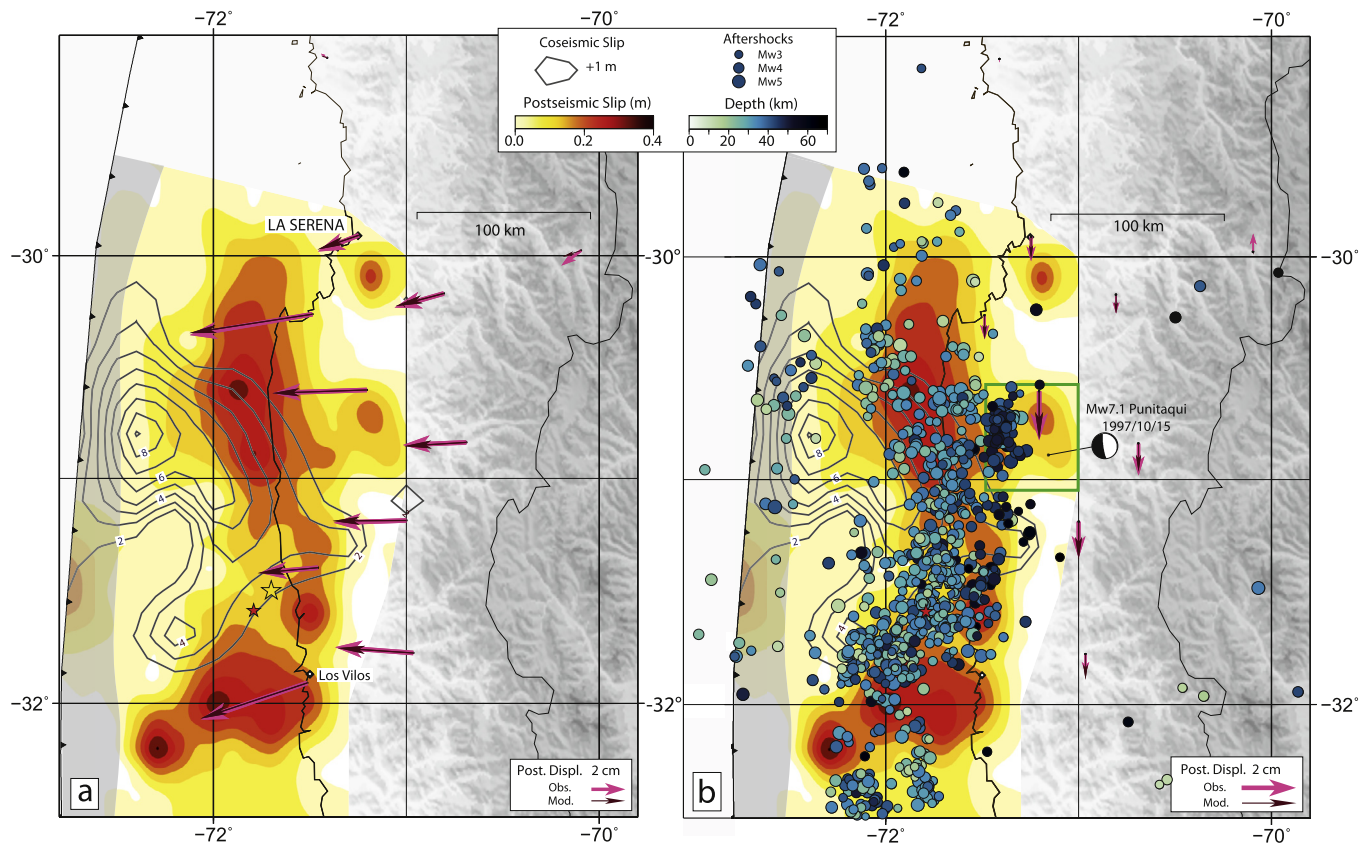| Damping coefficient	Contribution to the penalty function			M_0 (N m)	Mw	P (m m^2)
	GPS	InSAR	Damping			
cm10	0.539	0.399	6.24E−002	3.55E+021	8.30	8.20E+010
cm20	0.529	0.398	7.23E−002	3.35E+021	8.28	7.31E+010
cm30	0.511	0.396	9.27E−002	3.25E+021	8.27	6.73E+010
cm300	0.333	0.258	0.409	3.09E+021	8.26	6.02E+010

Fig. 7. Eleven days of postseismic displacements. a) Horizontal, b) vertical. Observed displacements (pink arrows), compared to the prediction of the best fit model (black arrows). The slip distribution is represented with the red color scale (m), grey contours represent the preferred coseismic slip distribution (+1 m). b) Dots represent aftershocks of Mw < 5 (CSN catalog), that occurred during the same period. The yellow star depicts the epicenter of the main shock, the red one the aftershock epicenter (Ruiz et al., 2016). The green rectangle highlights the area of denser seismicity where models show the maximum residuals. Localization of the Punitaqui earthquake from Engdahl and Villaseñor (2002), focal mechanism from USGS. The area of very low sensitivity is depicted by the grey area at the trench. (For interpretation of the references to color in this figure legend, the reader is referred to the web version of this article.)

four models have a significant component of deeper slip localized at ∼31.25°S, corresponding to the area where uplift is measured. The onland deformation associated the poorly resolved part of the inverted slip (i.e. with the component of slip hampered by the damping parameter) is small. Fig. S13 represents the diagonal terms of the resolution matrix for the four damping coefficients. Such resolution maps outline the areas where damping hampers the inverted signal. They are thus a direct representation of the areas where the slip predicted by the inversion is poorly resolved given the damping parameters (i.e. associated with low eigenvalues of $G^t \cdot C_d^{-1} \cdot G$). Although these models differ significantly, they all show similar residuals between measured and predicted coseismic offsets, with maximum horizontal residuals near Punitaqui and vertical residuals larger where slip deepens. The fit to the InSAR data is equivalent in the four models. They yield similar seismic moments, between 3.1×10^{21} N m and 3.5×10^{21} N m, comparable to the seismological estimate of 3.2×10^{21} N m (Finite fault model from USGS: https://earthquake.usgs.gov/archive/product/finite-fault/us20003k7a/us/1442454346406/web/20003k7a.fsp, Table 1). This might seem surprising because models with low damping seem to have more slip. However, high and localized slip in soft material (i.e. near the trench) is equivalent to a smoothed low slip zone in high shear modulus materials (i.e. deeper) in terms of moment. We therefore conclude that geodetic data constrain very well the magnitude and centroid location leaving space for interpretation on the distribution of slip.

The geometric moment (potency, which is the product of slip and rupture area) varies more drastically as it does not account for the variations in shear modulus. We find 8.20×10^{10} m m^2 for the

least damped model, vs 6×10^{10} m m^2 for the most damped one. Our potency is different from the estimate of the finite fault model from USGS (9.23×10^{10} m m^2), and generally lower, even for the least damped slip distribution.

5.1.2. Sensitivity of different data sets and their relative weight in the inversion

Different data sets yield different resolution or sensitivity to the slip distribution on the fault plane. Additionally, their weight in the inversion is crucial. An equal weight to an InSAR pixel and to a GPS point would inevitably lead to a model driven by InSAR data only (i.e. millions of pixels compared to tens of GPS markers only). Assigning a relative weight representative of the relative uncertainties and down-sampling the interferograms are standard procedure to address this problem. However, the down-sampling scheme and the estimated of uncertainties have an impact on the resolution.

Therefore, we compute the sensitivity defined as:

$$S = \text{diag}(G^t \cdot C_d^{-1} \cdot G) \qquad (2)$$

with G the Green's functions for the dip slip component and C_d the data covariance matrix (diagonal matrix of cGPS and sGPS uncertainties, and non-diagonal matrix for InSAR data, cf. section 2.2) following (Duputel et al., 2015). This sensitivity considers all data including the relative weights used in the inversion (Fig. S14). It shows lesser sensitivity on the shallowest part of the interface. Sensitivity is maximum between 50 and 15 km depth, reasonable, although reduced by a factor of 2, between 15 and 8 km, and almost null above. Therefore, terrestrial geodetic data cannot exclude the possibility of slip on the shallowest part of the interface,
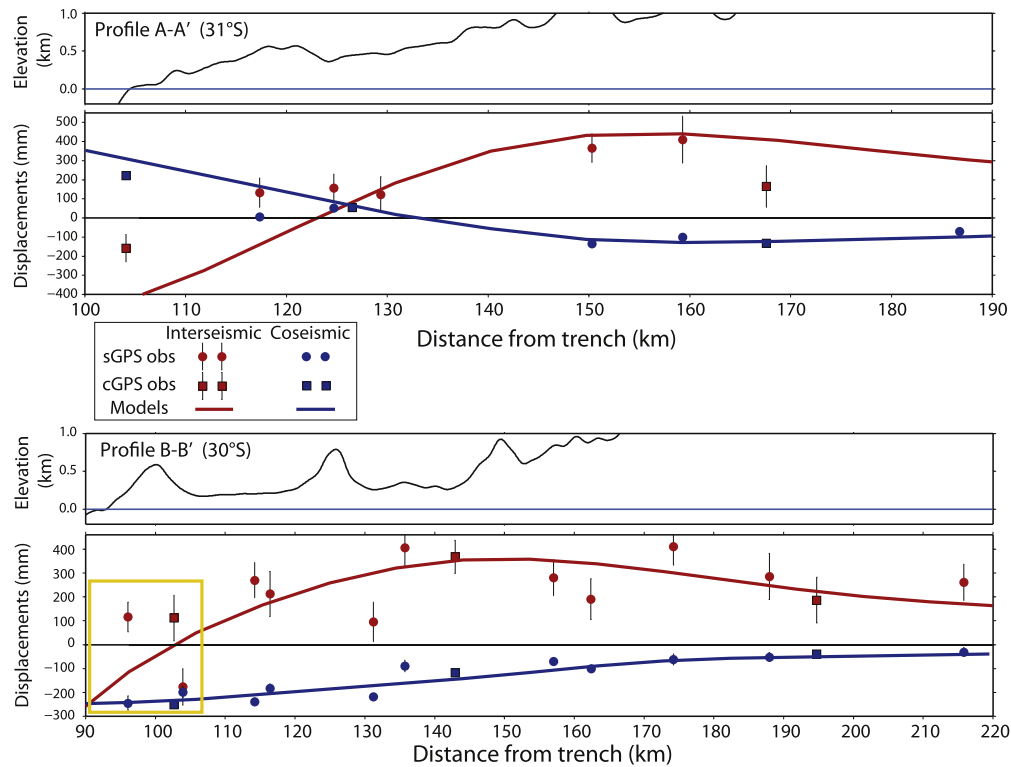
Fig. 8. Interplay between interseismic and coseismic deformation. Comparison of cumulated vertical interseismic displacements over 72 yr measured (red dots) and modeled (red curve from Métois et al., 2016, models were mostly constrained on the horizontal interseismic deformation between 2004 and 2012 and are here extrapolated over 72 yr, in mm) vs vertical coseismic displacements measured (blue dots) and modeled (blue curve), in mm. Profiles are represented on Fig. 2D. Topographic profiles are from ETOPO. (The yellow square highlights the area where the coseismic and interseismic models show both subsidence.) (For interpretation of the references to color in this figure legend, the reader is referred to the web version of this article.)

but hardly constrain it. A notable exception is the area near 31°S where sensitivity is slightly better where the coastline is closer to the trench and where the maximum displacements of 2 m are observed. Downweighting these two sites in the inversion leads to a shift of the area of maximum slip down to almost 20 km (Fig. S15). Apart for those two sGPS vectors, tsunami data alone may allow to constrain the shallow component of slip (e.g. Duputel et al., 2015; Melgar et al., 2016; Tilmann et al., 2016).

5.2. Inferences from the models

5.2.1. Shallow slip or not

Whether shallow slip is substantiated and whether the rupture actually broke to the surface is still debated. Some studies suggest that the rupture reached the sea-floor (e.g. Zhang et al., 2016). This question is particularly important with respect to tsunami-genic hazard since a strong shallow component of coseismic slip, a fortiori a rupture emerging at the trench, would trigger a strong tsunami. A maximum run up of 11 m was measured although in one location only (Aránguiz et al., 2016; Melgar et al., 2016). It was even described as an outlier by Aránguiz et al. (2016). Heights between 4 and 6 m were reported over a limited area (30.3–30°S) north of the rupture, which most likely resulted from local shoreline amplification (complex succession of peninsulas and bays). Otherwise, inundations remained below 4 m everywhere, consistent with the 3 m recorded at the Coquimbo tide gauge, with limited reported damages. Additionally, minor sea level elevation was reported at several tide gauges along the Japanese coast (0–30 cm) (ITIC, http://itic.ioc-unesco.org/index.php?option=com_content&view=category&layout=blog&id=2164&Itemid=2616). Similar heights were reported for the 1943 earthquakes, both in near and far field, including Japan (Beck et al., 1998; Lomnitz, 2004). Therefore, although a significant amount of shallow slip has most

probably occurred (our best model shows several meters of peak coseismic slip of 10 m at 10 km depth), the amount of slip reaching the trench remains uncertain. Because onland geodesy poorly constrain this portion of the interface, the slip distribution is strongly dependent on the model regularization, as shown by the slip distributions inverted with four different damping coefficients (section 5.1). Also, slip at slightly deeper depth can produce as much vertical deformation (if not more) as slip at the trench. A final and decisive argument could come from the presence/absence of outer-rise seismicity immediately after the main shock. It has been proposed that outer rise seismicity would follow megathrust earthquakes only when the rupture emerges at the trench (Sladen and Trévisan, 2016). Here, a few normal faulting out-rise aftershocks occurred (Tilmann et al., 2016), mostly located between 30 and 31°S. Therefore, the rupture might have reached the trench, in any case in the northernmost part of the rupture, where slip is maximum and shallowest.

5.2.2. Interplay between interseismic and coseismic deformation

Coseismic vertical offsets estimated on daily solution show a good anti-correlation with the interseismic vertical velocities: coseismic uplift due to deep slip occurs over an area subsiding over the interseismic period on profile A–A′ (Fig. 8, Métois et al., 2014, 2016). Further inland, coseismic subsidence coincides with interseismic uplift. Extrapolating the interseismic velocities measured before the Maule earthquake over 72 yr (the time elapsed since the equivalent earthquake of 1943), we find comparable displacements with opposite signs in this specific area (Fig. 8a, profile A–A′). On the northern profile B–B′, interpretation is less straight-forward (Fig. 8b). At sites further than 110 km from the trench, interseismic uplift anti-correlates with coseismic subsidence, but not at coastal sites. Along this profile near the coast, we measure coseismic subsidence and interseismic coastal subsidence is pre-

dicted by the elastic model inferred from pre-2010 GPS velocities. However, this model is mostly constrained by the more precisely determined horizontal deformation (Métois et al., 2014, 2016). Future studies will have to focus on developing new models able to better reconcile the horizontal and vertical component, which is currently not possible using simple elastic assumptions. Coseismic coastal subsidence at this latitude is a direct consequence of shallow slip, leaving a significant deep slip deficit. Because coupling is significant there, part of this deep slip deficit could be released by a significant deep aftershock. This would be similar to the 2012 Constitución event after the 2010 Maule megathrust earthquake, where the coastal station CONS subsided almost 40 cm because of the Mw8.8 earthquake, and uplifted about 12 cm due to the Constitución aftershock (Vigny et al., 2011; Ruiz et al., 2013). Still, on both profiles vertical coseismic displacements are smaller than the cumulative interseismic vertical displacements. If the interseismic coupling is stable over the whole seismic cycle, this difference could suggest that the 2015 Illapel earthquake did not fully release the deformation accumulated since the 1943 earthquake. However, the 2 m of co-seismic horizontal displacements measured at the coast near 31°S (profile A–A′) compensate the 72 yr of accumulation at a rate of 3 cm/yr. 50 km further inland, interseismic horizontal displacements over 72 yr are more than twice the coseismic displacements. The observed deficit of coseismic vertical and horizontal displacements inland could be balanced by post-seismic deformation along the deep part of the subduction interface (Trubienko et al., 2013), by subsequent earthquakes in this area, north and south of the rupture zone of the Illapel earthquake or by stress accumulation linked to a potential future 'supercycle' of large earthquakes. Note that the compensation of the coseismic displacements by interseismic displacements, which is the base for the above discussion is an acceptable concept only above the seismogenic part of the subduction interface. Further inland, postseismic displacements due to stress relaxation in the asthenosphere and in the low-viscosity channel become an important factor in the compensation of displacements through the seismic cycle and the 'elastic backslip' concept is no longer a proper approximation (Trubienko et al., 2013).

The observed deficit of coseismic displacements could also be the signature of a long term vertical effect of the interseismic period at the origin of long term topography building. In particular, elevated terraces are present at the same latitude as the area of maximum slip, between 30°s and 31°S, where slip is mostly shallow (Saillard et al., 2009). The precise mechanism at the origin of this apparent interplay between deformation during the seismic cycle and at geological time scales will have to be further investigated with more complicated, viscoelastic modeling of the seismic cycle.

5.2.3. North–south extension of the rupture

The northern limit of the rupture coincides with the presence of the Low Coupling Zone of La Serena revealed by 10 yr of GPS measurements (Métois et al., 2012). This zone coincides with the termination of all recent and historical ruptures, suggesting a potential control of earthquake propagation by an aseismic barrier. The southern limit of the rupture is more difficult to relate to physical considerations. Recent GPS measurements highlight an almost continuous and highly coupled Metropolitan segment between 34°S and 30°S, with only a very small and local decrease of coupling near 32°S [Métois et al., 2012, 2016, Fig. S7]. Unfortunately, the Valparaiso region (between 32°S and 34°S) was poorly covered with GPS markers prior to the Maule earthquake of 2010, and the analysis of the segmentation of the Metropolitan segment from the GPS inferred coupling is incomplete. We propose here an hypothesis to explain why the rupture stopped at the latitude of Los Vilos (32°S).

This limit overlaps with the area where the Juan Fernandez Ridge enters the subduction (Fig. 4, Yáñez et al., 2001). Along the Nankai Trough of Japan, a direct evidence of subducting seamounts generating Very Low Frequency Earthquake activity together with a low slip deficit rate have been reported (Yokota et al., 2016). Subducting seamounts and more generally topographical fault irregularities may cause heterogeneities in the stress field because they produce damage in the surrounding media (Wang and Bilek, 2011, 2014) or because they lower the effective friction (Fagereng and den Hartog, 2016). Therefore, subducting seamounts or ridges tend to act as megathrust rupture barrier, even though such barriers may sometimes be overstepped by the dynamic stress perturbation induced by the earlier phase of the rupture. The persistence and the ability of this barrier to arrest ruptures remains a fundamental question as the 1880, 1943 and 2015 Mw∼8+ ruptures stopped there but preseismic stresses, dynamic stresses and/or rheology allowed the 1730 Mw∼9 earthquake to go through.

5.2.4. Punitaqui anomaly

All tests presented in this study consistently show relatively large residuals (i.e. horizontal component of GPS and reconstructed InSAR) in the Punitaqui area (near 31°S, 71°W). This feature does not depend on model parameters (distribution of elastic properties, damping, rake angle). Therefore, it must be related to an additional tectonic phenomena we do not account for in our modeling. Remarkably, this precise area, close to the epicenter of the intraplate slab-push Punitaqui earthquake of 1997 (Gardi et al., 2006), shows a stronger seismic activity during the first 11 days following the earthquake than the rest of the region (Fig. 6-b, green rectangle). Therefore, this intraplate fault could have been reactivated during the Illapel earthquake, generating a high postseismic activity and inducing deformation that slip on the subduction interface cannot reproduce. This hypothesis is also supported by the presence of intraplate intermediate depth or crustal earthquakes in this precise area (e.g. Ruiz et al., 2016). Unfortunately, continuous GPS data will not allow to study more closely this phenomenon because the network is too sparse. Only two stations (CMBA in Combarbala and OVLL in Ovalle) are operating nearby but their locations are not appropriate. InSAR time series and precise focal mechanisms determination during the post-seismic period will allow the verification of this hypothesis.

6. Conclusions

In this study, we showed how survey data is fundamental to constrain slip at shallower depth than with cGPS alone. Only these data, and in particular the sites along the coast in front of the rupture which exhibit a peak co-seismic deformation of ∼2 m require really shallow slip. Because the network is too sparse, cGPS data do not allow such resolution. We find the rake of slip during the earthquake is aligned with plate convergence direction, leading to two distinct conclusions. First, there is no strike-slip deficit. Second, the exact location of the main slip zone determined by the inversion depends on the rake of the slip. A slip perpendicular to the trench locates the bulk of the rupture slightly south of where we locate it using an oblique slip (because of the angle with which the slip on the fault plane will "pull" the on-land vectors). We argue that the main slip zone of our model is better located using the oblique slip assumption. This leads to note a striking coincidence between the main slip zone and coastal morphology: large earthquakes are bounded by two main bathymetric features (JFR and CFZ), but the maximum slip zone is located, where high coastal topography with elevated terraces is observed. This is additional evidence for a potential relationship between the seismic cycle and the long-term building of coastal topography. Co-seismic slip does not completely release strain that has been accumulated

during the interseismic period, at least based on the vertical component. Apart from the moment rate function which seems to be significantly shorter in 1943 than 2015 (30 s compared to 70 s) (Beck et al., 1998; Tilmann et al., 2016), there is no clear evidence that 2015 is really different (and larger) than 1943. Therefore, the 2015 Illapel earthquake appears to follow the pattern of characteristic megathrust earthquakes occurring every ∼70 yr along this segment. This earthquake may have released the accumulated deformation since the last earthquake of 1943 closing the seismic gap related to the 1880–1943–2015 cycle.

Seismic hazard following the Illapel event of 2015 relies on two compatible scenarios. First, following the Maule and Illapel earthquake, a continuing propagation towards the north would lead to a rupture along the next segment of the subduction: the Atacama segment. This portion of the subduction megathrust is mature for a magnitude 8+ earthquake as no significant event occurred there since the 1922 Mw8.7 earthquake. Furthermore, this segment is locked and highly coupled (Métois et al., 2012, 2016). The 1922 earthquake ruptured a more than 350 km long segment, from the Punta Choros (∼29°S) up to Chanaral (∼26.5°S), destroying several cities. It resulted in a significant tsunami which traveled more than 1 km inland and was more damaging than the earthquake itself in several coastal cities, an in particular in La Serena (Beck et al., 1998; Comte et al., 2002). The second scenario, and both could occur, involves the occurrence of a giant earthquake similar to the historic event of 1730 rupturing simultaneously several segments from Concepcion (37°S) to at least La Serena (30°S) and possibly higher north (Udias et al., 2012). Such an earthquake would re-rupture segments of the 2010 Maule earthquake, the 1906 Valparaiso earthquake and finally the 2015 Illapel event. Such a giant earthquake, following a 300-yr super-cycle would affect the whole central Chile and is associated with an extremely high tsunamigenic hazard. In this scenario, comparable to the super-cycle of Sumatra (Sieh et al., 2008) and Ecuador (Nocquet et al., 2016), the 2010 and 2015 ruptures would have distributed stresses for an upcoming giant earthquake, rather than dissipated the deformation accumulated since 1730 rather than 1835 and 1943 respectively. Nevertheless, the first scenario appears more likely to occur. While the 2015 earthquake arguably was too small to alter the deformation budget for the whole region substantially, the 2010 Maule earthquake might have been large enough to reduce the deformation deficit along a significant block of the margin. Furthermore, both events seem to account for most of the local deformation deficit accumulated since the last major earthquakes in their respective segments (i.e. 1835 and 1943), favoring the first scenario.

Acknowledgements

Appendix A. Supplementary material

Supplementary material related to this article can be found online at http://dx.doi.org/10.1016/j.epsl.2017.04.010.

References

Angermann, D., Klotz, J., Reigber, C., 1999. Space geodetic estimation of the Nazca–South America Euler vector. Earth Planet. Sci. Lett. 171, 329–334.

Aránguiz, R., González, G., González, J., Catalán, P.A., Cienfuegos, R., Yagi, Y., et al., 2016. The 16 September 2015 Chile tsunami from the post-tsunami survey and numerical modeling perspectives. Pure Appl. Geophys. 173 (2), 333–348.

Beck, S., Barrientos, S., Kausel, E., Reyes, M., 1998. Source characteristics of historic earthquakes along the central Chile subduction zone. J. South Am. Earth Sci. 11, 115–129.

Comte, D., Haessler, H., Dorbath, L., Pardo, M., Monfret, T., Lavenu, A., Pontoise, B., Hello, Y., 2002. Seismicity and stress distribution in the Copiapo, northern Chile subduction zone using combined on- and off-shore seismic observations. In: Subduction Zone Structure and Megathrust Earthquakes. Phys. Earth Planet. Inter. 132 (1–3), 197–217.

Contreras-Reyes, Eduardo, Carrizo, Daniel, 2011. Control of high oceanic features and subduction channel on earthquake ruptures along the Chile–Peru subduction zone. Phys. Earth Planet. Inter. (ISSN 0031-9201) 186 (1–2), 49–58. http://dx.doi.org/10.1016/j.pepi.2011.03.002.

Duputel, Z., Rivera, L., Kanamori, H., Hayes, G., 2012. W phase source inversion for moderate to large earthquakes (1990–2010). Geophys. J. Int. 189 (2), 1125–1147.

Duputel, Z., Jiang, J., Jolivet, R., Simons, M., Rivera, L., Ampuero, J.P., et al., 2015. The Iquique earthquake sequence of April 2014: Bayesian modeling accounting for prediction uncertainty. Geophys. Res. Lett. 42 (19), 7949–7957.

Dziewonski, A.M., Anderson, D.L., 1981. Preliminary reference earth model. Phys. Earth Planet. Inter. 25 (4), 297–356.

Engdahl, E.R., Villaseñor, A., 2002. 41 Global seismicity: 1900–1999. Int. Geophys. 81, 665–XVI.

Fagereng, Åke, den Hartog, Sabine A.M., 2016. Subduction megathrust creep governed by pressure solution and frictional-viscous flow. Nat. Geosci. 10, 51–57. http://dx.doi.org/10.1038/ngeo2857.

Feng, W., Samsonov, S., Tian, Y., Qiu, Q., Li, P., Zhang, Y., Deng, Z., Omari, K., 2017. Surface deformation associated with the 2015 Mw 8.3 Illapel earthquake revealed by satellite-based geodetic observations and its implications for the seismic cycle. Earth Planet. Sci. Lett. (ISSN 0012-821X) 460, 222–233. http://dx.doi.org/10.1016/j.epsl.2016.11.018.

Gardi, A., Lemoine, A., Madariaga, R., Campos, J., 2006. Modeling of stress transfer in the Coquimbo region of central Chile. J. Geophys. Res. 111, B04307. http://dx.doi.org/10.1029/2004JB003440.

Grandin, R., Klein, E., Métois, M., Vigny, C., 2016. Three-dimensional displacement field of the 2015 Mw8. 3 Illapel earthquake (Chile) from across- and along-track Sentinel-1 TOPS interferometry. Geophys. Res. Lett. 43 (6), 2552–2561.

Hayes, G.P., Wald, D.J., Johnson, R.L., 2012. Slab1. 0: a three-dimensional model of global subduction zone geometries. J. Geophys. Res., Solid Earth 117(B1).

Heidarzadeh, M., Murotani, S., Satake, K., Ishibe, T., Gusman, A.R., 2016. Source model of the 16 September 2015 Illapel, Chile, Mw 8.4 earthquake based on teleseismic and tsunami data. Geophys. Res. Lett. 43, 643–650. http://dx.doi.org/10.1002/2015GL067297.

Herring, T., King, R., McClusky, S.C., 2010a. GAMIT: GPS Analysis at MIT, Release 10.4.

Herring, T., King, R., McClusky, S.C., 2010b. GLOBK: Global Kalman Filter VLBI and GPS Analysis Program, Release 10.4.

Hill, E., Borrero, J.C., Huang, Z.H., Qiu, Q., Banerjee, P., Natawidjadja, D., Elosegui, P., Fritz, H.M., Suwargadi, B., Pranantyo, I., Li, L.L., Macpherson, K., Skanavis, V., Synolakis, C., Sieh, K., 2012. The 2010 Mw 7.8 Mentawai earthquake: very shallow source of a rare tsunami earthquake determined from tsunami field survey and near-field GPS data. J. Geophys. Res. 117, B06402. http://dx.doi.org/10.1029/2012JB009159.

Jolivet, R., Simons, M., Agram, P.S., Duputel, Z., Shen, Z.K., 2015. Aseismic slip and seismogenic coupling along the central San Andreas Fault. Geophys. Res. Lett. 42 (2), 297–306. http://dx.doi.org/10.1002/2014GL062222.

Klein, E., Fleitout, L., Vigny, C., Garaud, J.D., 2016. Afterslip and viscoelastic relaxation model inferred from the large-scale post-seismic deformation following the 2010 Mw 8.8 Maule earthquake (Chile). Geophys. J. Int. 205 (3), 1455–1472.

Lemoine, A., Madariaga, R., Campos, J., 2002. Slab-pull and slab-push earthquakes in the Mexican, Chilean and Peruvian subduction zones. Phys. Earth Planet. Inter. 132 (1), 157–175.

Lohman, R.B., Simons, M., 2005. Some thoughts on the use of InSAR data to constrain models of surface deformation: noise structure and data downsampling. Geochem. Geophys. Geosyst. 6 (1), Q01007. http://dx.doi.org/10.1029/2004GC000841.

Lomnitz, C., 2004. Major earthquakes of Chile: a historical survey, 1535–1960. Seismol. Res. Lett. 75, 368–378.

Melgar, D., Fan, W., Riquelme, S., Geng, J., Liang, C., Fuentes, M., et al., 2016. Slip segmentation and slow rupture to the trench during the 2015, Mw8.3 Illapel, Chile earthquake. Geophys. Res. Lett. 43 (3), 961–966.

Métois, M., Vigny, C., Socquet, A., 2012. Interseismic coupling, segmentation and mechanical behavior of the central Chile subduction zone. J. Geophys. Res. 662, 120–131.

Métois, M., Vigny, C., Socquet, A., Delorme, A., Morvan, S., Ortega, I., Valderas-Bermejo, M.-C., 2014. GPS-derived interseismic coupling on the subduction and

seismic hazards in the Atacama region, Chile. Geophys. J. Int. 196, 644–655. http://dx.doi.org/10.1093/gji/ggt418.

Métois, M., Vigny, C., Socquet, A., 2016. Interseismic coupling, megathrust earthquakes and seismic swarms along the Chilean subduction zone (38°–18°S). Pure Appl. Geophys. 173 (5), 1431–1449.

Nocquet, J.M., Jarrin, P., Vallée, M., Mothes, P.A., Grandin, R., Rolandone, F., et al., 2016. Supercycle at the Ecuadorian subduction zone revealed after the 2016 Pedernales earthquake. Nat. Geosci. 10, 145–149. http://dx.doi.org/10.1038/ngeo2864.

Rivera, Efrain, 2015. Procesamiento y analisis de motogramas de terremotos de subduccion chilenos. Master thesis in geophysics, Universidad de Chile, Facultad de Ciencias Fisicas y Matematicas, Departamento de Geofisica.

Ruiz, S., Grandin, R., Dionicio, V., Satriano, C., Fuenzalida, A., Vigny, C., et al., 2013. The Constitución earthquake of 25 March 2012: a large aftershock of the Maule earthquake near the bottom of the seismogenic zone. Earth Planet. Sci. Lett. 377, 347–357.

Ruiz, S., Klein, E., del Campo, F., Rivera, E., Poli, P., Métois, M., Vigny, C., Baez, J., Varges, G., Leyton, F., Madariaga, R., Fleitout, L., 2016. The seismic sequence of the 16 September 2015, Illapel Mw 8.3 earthquake. Seismol. Res. Lett. http://dx.doi.org/10.1785/0220150281.

Saillard, M., Hall, S.R., Audin, L., Farber, D.L., Hérail, G., Martinod, J., et al., 2009. Nonsteady long-term uplift rates and Pleistocene marine terrace development along the Andean margin of Chile (31°S) inferred from 10 Be dating. Earth Planet. Sci. Lett. 277 (1), 50–63.

Shrivastava, M.N., González, G., Moreno, M., Chlieh, M., Salazar, P., Reddy, C.D., Báez, J.C., Yáñez, G., González, J., de la Llera, J.C., 2016. Coseismic slip and afterslip of the 2015 Mw 8.3 Illapel (Chile) earthquake determined from continuous GPS data. Geophys. Res. Lett. 43, 10,710–10,719. http://dx.doi.org/10.1002/2016GL070684.

Sieh, K., Natawidjaja, D., Meltzner, A., Shen, C.-C., Cheng, H., Li, K.S., Suwargadi, B., Galetzka, J., Philibosian, B., Edwards, R., 2008. Earthquake supercycles inferred from sea-level changes recorded in the corals of West Sumatra. Science 322, 1674.

Sladen, A., Trévisan, J., 2016. Detecting the surface rupture of subduction earthquakes from aftershocks. In: AGU Fall Meeting 2016.

Tilmann, F., Zhang, Y., Moreno, M., Saul, J., Eckelmann, F., Palo, M., Deng, Z., Babeyko, A., Chen, K., Baez, J.C., Schurr, B., Wang, R., Dahm, T., 2016. The 2015 Illapel earthquake, central Chile: a type case for a characteristic earthquake? Geophys. Res. Lett. 43, 574–583. http://dx.doi.org/10.1002/2015GL066963.

Trubienko, O., Fleitout, L., Garaud, J.-D., Vigny, C., 2013. Interpretation of interseismic deformations and the seismic cycle associated with large subduction earthquakes. Tectonophysics 589, 126–141. http://dx.doi.org/10.1016/j.tecto.2012.12.027.

Udias, A., Madariaga, R., Buforn, E., Muñoz, D., Ros, M., 2012. The large Chilean historical earthquakes of 1647, 1657, 1730, and 1751 from contemporary documents. Bull. Seismol. Soc. Am. 102 (4), 1639.

Vigny, C., Rudloff, A., Ruegg, J.C., Madariaga, R., Campos, J., Alvarez, M., 2009. Upper plate deformation measured by GPS in the Coquimbo Gap, Chile. Phys. Earth Planet. Inter. 175 (1), 8695.

Vigny, C., et al., 2011. The 2010 Mw 8.8 Maule megathrust earthquake of Central Chile, monitored by GPS. Science 332 (6036), 1417–1421.

Wang, K., Bilek, S.L., 2011. Do subducting seamounts generate or stop large earthquakes? Geology 39 (9), 819–822.

Wang, K., Bilek, S.L., 2014. Invited review paper: fault creep caused by subduction of rough seafloor relief. Tectonophysics 610, 1–24.

Yáñez, G.A., Ranero, C.R., Huene, R., Díaz, J., 2001. Magnetic anomaly interpretation across the southern central Andes (32–34°S): the role of the Juan Fernández Ridge in the late Tertiary evolution of the margin. J. Geophys. Res., Solid Earth 106 (B4), 6325–6345.

Yokota, Y., Ishikawa, T., Watanabe, S.I., Tashiro, T., Asada, A., 2016. Seafloor geodetic constraints on interplate coupling of the Nankai Trough megathrust zone. Nature 534, 374–377. http://dx.doi.org/10.1038/nature17632.

Zhang, Y., Zhang, G., Hetland, E.A., Shan, X., Wen, S., Zuo, R., 2016. Coseismic fault slip of the September 16, 2015 Mw 8.3 Illapel, Chile earthquake estimated from InSAR data. Pure Appl. Geophys. 173 (4), 1029–1038.